Effect of Turbulence Parameterization on Assessment of Cloud Organization

LUIZ A. T. MACHADO

Instituto Nacional de Pesquisas Espaciais, Centro de Previsão de Tempo e Estudos Climáticos, Cachoeira Paulista, São Paulo, Brazil

JEAN-PIERRE CHABOUREAU

Laboratoire d'Aérologie, University of Toulouse/CNRS, Toulouse, France

(Manuscript received 29 November 2014, in final form 20 April 2015)

ABSTRACT

This study evaluates the cloud and rain cell organization in space and time as forecasted by a cloud-resolving model. The forecast fields, mainly describing mesoscale convective complexes and cold fronts, were utilized to generate synthetic satellite and radar images for comparison with Meteosat Second Generation and S-band radar observations. The comparison was made using a tracking technique that computed the size and lifetime of cloud and rain distributions and provided histograms of radiative quantities and cloud-top height. The tracking technique was innovatively applied to test the sensitivity of forecasts to the turbulence parameterization. The simulations with 1D turbulence produced too many small cloud systems and rain cells with a shorter lifetime than observed. The 3D turbulence simulations yielded size and lifetime distributions more consistent with the observations. As shown for a case study, 3D turbulence yielded longer mixing length, larger entrainment, and stronger turbulence kinetic energy inside clouds than 1D turbulence. The simulation with 3D turbulence had the best scores in high clouds. These features suggest that 1D turbulence did not produce enough entrainment, allowing the formation of more small cloud and rain cells than observed. Further tests were performed on the sensitivity to the mixing length with 3D turbulence. Cloud organization was very sensitive to in-cloud mixing length and the use of a very small value increased the number of small cells, much more than the simulations with 1D turbulence. With a larger in-cloud mixing length, the total number of cells, mainly the small ones, was strongly reduced.

1. Introduction

Meteorological models are increasingly being used at higher spatial and temporal resolution. Today's computer power makes it possible to run models at scales of a few kilometers in operational mode and at scales of a few hundred meters for research purposes. Short-range forecasting of precipitation at high resolution has important applications in several areas of benefit to society. The increasing frequency of precipitation extremes with climate change (Meehl et al. 2000) reinforces the need for such forecasts, able to predict high rates of precipitation and produced by models running at high resolution. However, high-resolution models representing the mesoscale and larger convective-scale convective dynamics explicitly still need to be improved and evaluated.

It is well known that numerical models have difficulty in reproducing precipitation features precisely. This is particularly true for the tropics where substantial errors still occur (Kidd et al. 2013). A comparison of precipitation between model simulation and observation normally cannot be performed point by point because of the limited predictability and the large variability of the rainfall field at small spatial and temporal scales. Another drawback is generally the lack of a rain gauge network at high resolution in the region of interest. The most convenient solution for comparing simulated and observed cloud and rainfall fields is to use satellite and radar data, from which essential information on cloud processes can be obtained. Machado et al. (2009) described the use of the difference between infrared window and water vapor channels to estimate penetrative

Corresponding author address: Luiz Augusto Toledo Machado, Instituto Nacional de Pesquisas Espaciais, Centro de Previsão de Tempo e Estudos Climáticos, Rodovia Pres. Dutra, km 40, Cachoeira Paulista, São Paulo 12630-000, Brazil.
E-mail: luiz.machado@cptec.inpe.br

DOI: 10.1175/MWR-D-14-00393.1

cloud and cloud lightning activity. Rosenfeld et al. (2008) used a combination of satellite channels to retrieve vertical profiles of cloud particle effective radius and thermodynamic phase. Chong et al. (1987) retrieved the kinematic structure using dual-Doppler radar.

As an alternative to the use of satellite and radar retrievals, synthetic images can be computed from model outputs using radiative transfer codes and directly compared to observations. In this way, the skill of the model in reproducing the cloud properties at high space–time resolution can be estimated (see Ringer et al. 2003; Chaboureau and Pinty 2006; Meirold-Mautner et al. 2007, among many others). The evaluation of a specific satellite brightness temperature or a channel combination or the three-dimensional field observed by radar are some of the variables that can be used in the comparison between a synthetic field produced from high-resolution models and observations at the scale of a few kilometers (satellite) to a few hundred meters (radar).

Precipitation field estimation by numerical weather forecast models needs to make considerable progress before it can be used for streamflow forecasting (Shrestha et al. 2013). Recently, Varble et al. (2011) compared nine cloud-resolving model simulations with scanning radar reflectivity and satellite infrared brightness temperature observations. Although the study was applied for only a 6-day active monsoon period during the Tropical Warm Pool–International Cloud Experiment (TWP-ICE), they concluded that models, in general, overestimated convective area and rainfall and underestimated stratiform rainfall. Varble et al. (2014), studying an intense mesoscale convective system observed during TWP-ICE, showed that the high bias on simulated convective area was partly a result of overly intense updrafts. Negri et al. (2014) checked the principal components obtained from synthetic and observed satellite images to evaluate their space and time variability. They showed that the cloud-resolving model captured the main modes of cloud cover variability well. However, the model produced many more cloud systems than observed by Meteosat Second Generation (MSG). Recently, Caine et al. (2013) compared high-resolution simulations with radar data over northern Australia and found that the model produced smaller, taller rainfall cells (as defined by contiguous areas of high reflectivity) than were observed. Similar results, albeit with a different model running over the southern United Kingdom, were also found by Hanley et al. (2015).

The reasons for these deficiencies are not well established. They may include a poor description of the three-dimensional initial field and some systematic model errors. In particular, the strong sensitivity of high-resolution simulations to the microphysical parameterization is often pointed out as a model limitation [see Morrison and Grabowski (2007) for an evaluation of different microphysical models]. Another very important process that controls the turbulent mixing between a cloud and its environment is entrainment. As such, it is one of the most sensitive and important unknown parameters in deep convective schemes (Mapes and Neale 2011). Wang et al. (2007), Wu et al. (2009), and Lu et al. (2013) are some of several authors addressing the entrainment effect on cloud formation, evolution, and microphysical properties. At the kilometer scale, entrainment is partly represented by the subgrid turbulence scheme as shown for the boundary layer by Honnert et al. (2011). So a good representation of the turbulence is essential in the description of cloud processes and cloud space–time organization. The increase in boundary layer turbulent kinetic energy (TKE) facilitates convection by helping to raise parcels to their level of free convection. Conversely, high entrainment can act to inhibit the convective processes, thus delaying the transition from shallow to deep convection. So far, very few studies have focused on the effect of turbulence on cloud organization.

At kilometer scale, the motion within clouds remains insufficiently resolved. This was shown by several sensitivity studies of deep convective storms to the horizontal resolution (e.g., Bryan et al. 2003; Khairoutdinov et al. 2009; Caine et al. 2013; Dauhut et al. 2015). They all found a marked sensitivity of deep convection to the grid spacing. In particular, Caine et al. (2013) found that reducing the grid spacing (from 1250 to 417 m) reduced the overestimation in height and size of the convective cells. Further, a grid spacing of the order of 100 m appears to be necessary for resolving most of the kinetic energy contained in the largest eddies. These results point out the need for correct parameterization of the subgrid turbulence at kilometer scale. A few recent studies investigated the dependence of deep convection on the subgrid turbulence. Among them, Verrelle et al. (2015) performed idealized simulations of thunderstorms. They showed that a full 3D turbulence scheme produced more mixing than its 1D counterpart, even with grid spacing as coarse as 2 km. Hanley et al. (2015) investigated the sensitivity of storm morphology to the mixing length used in the subgrid turbulence scheme. They found an increase in the number of small storms with a decrease in subgrid mixing length.

These recent studies of cloud-resolving models point out the model deficiencies in describing the space–time cloud organization, the high cloud top of small convective cells, and the dependence on a specific model setup. Here, we examine the representation of turbulence in a cloud-resolving model by looking at its impact on the cloud organization in comparison with satellite and

radar observations. The dataset employed in this study was collected during one of the seven field campaigns of the CHUVA project. CHUVA, meaning "rain" in Portuguese, is the acronym for the Cloud Processes of the Main Precipitation Systems in Brazil: A Contribution to Cloud-Resolving Modeling and to the Global Precipitation Measurement (GPM) [see Machado et al. (2014) for a detailed description]. This study uses data collected in the CHUVA-SUL campaign, in Santa Maria Rio Grande do Sul State, in the south of Brazil, from 15 November to 15 December 2012. This is a region with a very high frequency of mesoscale convective systems (Salio et al. 2007) and is close to northern Argentina and southern Paraguay where severe hailstorms occur globally most often (Cecil and Blankenship 2012). The present article describes a new methodology for comparing simulations with satellite and radar observations using a tracking technique. This new methodology allows us to evaluate cloud organization in space and time and to test the effect of turbulence on the cloud organization.

Section 2 describes the simulations and the verification approach. Section 3 details the impact of the turbulence scheme in 1D and 3D mode for a case study. Section 4 discusses the statistical effect of 1D and 3D turbulence on all the simulations in terms of brightness temperature distribution and cloud space and time organization. Section 5 presents sensitivity experiments changing the in-cloud mixing length used in the 3D turbulence scheme and its effects on the cloud organization and the turbulent kinetic energy. Finally, section 6 summarizes our main findings.

2. Model and evaluation approach

a. *Méso-NH simulations*

During the CHUVA SUL campaign, the Méso-NH model (Lafore et al. 1998) version 4.9 was run using the two-way interactive grid-nesting method (Stein et al. 2000) with two nested grids: a horizontal grid mesh of 10 and 2 km and a vertical grid with 62 levels with a spacing varying from 60 m near the surface to 600 m at the model top at 25-km altitude. The initial and boundary conditions were provided by European Centre for Medium-Range Weather Forecasts (ECMWF) analysis and forecasts issued at 1200 UTC each day, from which the model was run for 36 h. The model includes parameterizations for turbulence (Cuxart et al. 2000), subgrid shallow convection (Pergaud et al. 2009), mixed-phase microphysics (Pinty and Jabouille 1998), and subgrid cloud cover and condensate content (Chaboureau and Bechtold 2005). The radiative scheme employed was the Rapid Radiative Transfer Model (Mlawer et al. 1997) for longwave radiation and the two-stream formulation originally employed by Fouquart and Bonnel (1986) for shortwave radiation. The convection scheme of Kain and Fritsch (1993), adapted to the Méso-NH model by Bechtold et al. (2001), was activated for the 10-km grid, while no deep convection parameterization was used for the 2-km grid (simulation using 500 by 500 grid points, see the domain in Fig. 1). From the model outputs, satellite brightness temperatures were computed using the Radiative Transfer for the Television and Infrared Observation Satellite (TIROS) Operational Vertical Sounder (TOVS) (RTTOV, version 8.7) (Saunders et al. 2005) as shown by Chaboureau et al. (2008) among others. Radar reflectivity was simulated using the methodology described by Richard et al. (2003).

The turbulence scheme implemented in Méso-NH by Cuxart et al. (2000) uses a 1.5-order closure based on mixing length and a prognostic equation for the subgrid-scale TKE with variables conserved for moist, nonprecipitating processes (the liquid-water potential temperature θ_l and the nonprecipitating total water mixing ratio $r_{\rm np}$). The TKE equation, which represents the isotropic part of the Reynolds stress tensor, reads as

$$\frac{\partial e}{\partial t} = -\frac{1}{\rho_{\rm ref}}\frac{\partial(\rho_{\rm ref} e\overline{u_i})}{\partial x_j} - \overline{u_i' u_j'}\frac{\partial \overline{u_i}}{\partial x_j} + \frac{g}{\theta_{\rm vref}}\overline{u_3'\theta_v'} + \frac{1}{\rho_{\rm ref}}\frac{\partial}{\partial x_j}\left(C_{2\rm m}\rho_{\rm ref} L e^{1/2}\frac{\partial e}{\partial x_j}\right) - C_\varepsilon\frac{e^{3/2}}{L}, \quad (1)$$

where e is the TKE; u_i is the ith component of the velocity; θ_v is the virtual potential temperature; $\rho_{\rm ref}$ and $\theta_{\rm vref}$ are the density and virtual potential temperature of the reference state, respectively; g is the gravitational acceleration; $C_{2\rm m}$ and C_ε are closure constants; and L the mixing length. Bars and primes denote means and turbulent components, respectively.

All the other second-order moments such as fluxes and the anisotropic part of the Reynolds stress tensor are diagnosed from the gradients of the resolved prognostic variables as

$$\overline{u_i' u_j'} = \frac{2}{3}\delta_{ij} e - \frac{4}{15}\frac{L}{C_m} e^{1/2}\left(\frac{\partial \overline{u_i}}{\partial x_j} + \frac{\partial \overline{u_j}}{\partial x_i} - \frac{2}{3}\delta_{ij}\frac{\partial \overline{u_n}}{\partial x_n}\right), \quad (2)$$

$$\overline{u_i'\theta_l'} = -\frac{2}{3}\frac{L}{C_s} e^{1/2}\frac{\partial \overline{\theta_l}}{\partial x_i}\varphi_i, \quad (3)$$

$$\overline{u_i' r_{\rm np}'} = -\frac{2}{3}\frac{L}{C_h} e^{1/2}\frac{\partial \overline{r_{\rm np}}}{\partial x_i}\psi_i, \quad (4)$$

where δ_{ij} is the Kronecker delta tensor; the Einstein summation convention applies for subscripts n, φ_i, and ψ_i are stability functions; and C_s, C_h, and C_m are constant

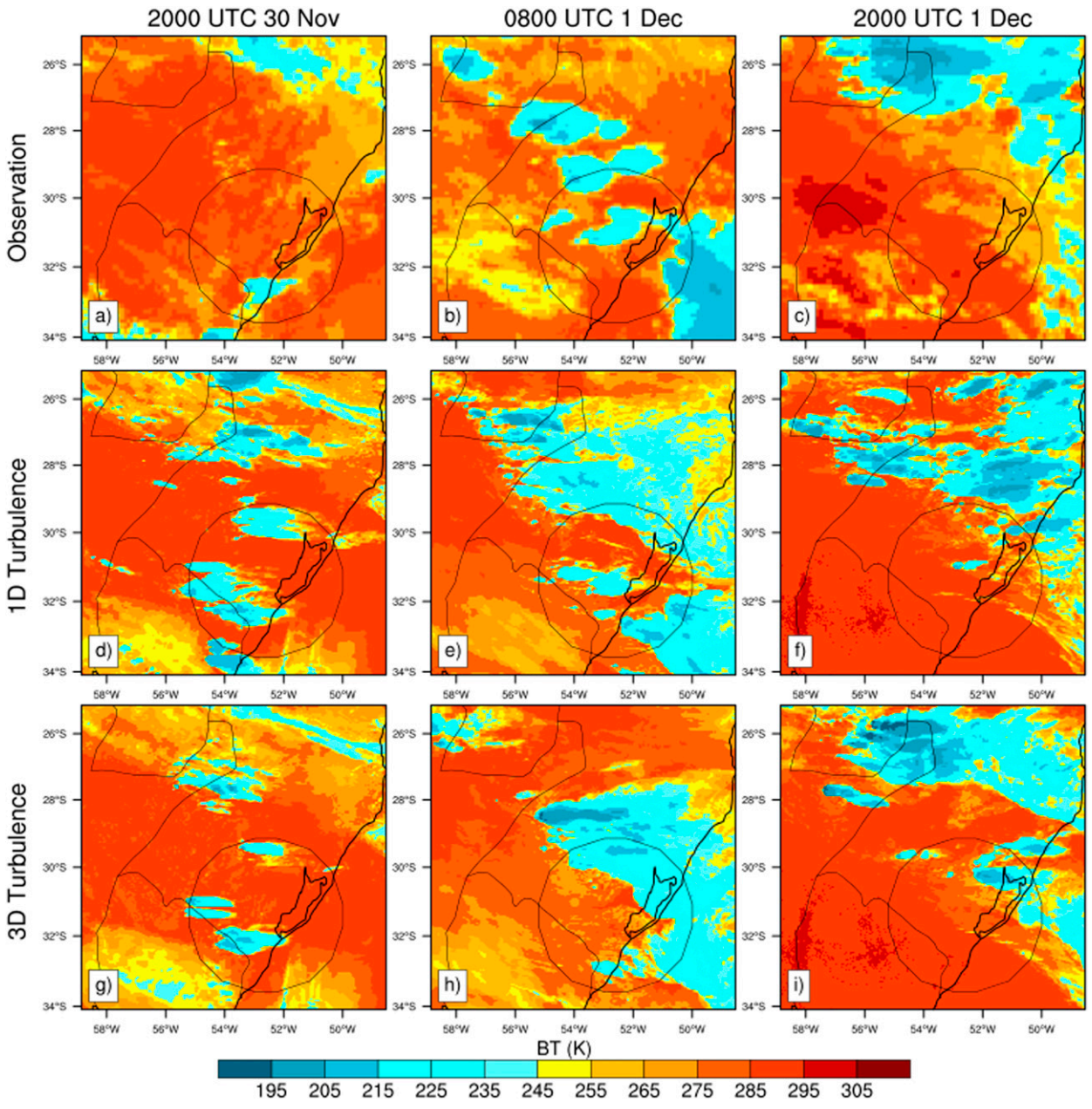

FIG. 1. MSG brightness temperature at 10.8 μm for (a)–(c) observation; (d)–(f) simulation with 1D turbulence; and (g)–(i) simulation with 3D turbulence for Julian day 335 at (a),(d),(g) 2000 UTC 30 Nov; (b),(e),(h) 0800 UTC 1 Dec; and (c),(f),(i) 2000 UTC 1 Dec. The circle shows the maximum range of the radar (250 km).

[see Cuxart et al. (2000) for further details]. The scheme can be used in both large-eddy and mesoscale simulations with the same set of closure constants.

For large-eddy simulations, the turbulence scheme is used in its complete formulation, the 3D mode. It is assumed that the most energetic parameterized eddies are just a little smaller than the grid spacing, hence the so-called Deardorff mixing length, which equals the grid size limited by the thermal stability:

$$L = (\Delta x \Delta y \Delta z)^{1/3}. \tag{5}$$

For mesoscale simulations, the turbulence scheme is usually set in 1D mode. In that case, it is assumed that the horizontal gradients and turbulent fluxes are negligible compared to their vertical counterparts. In other words, only the sources associated to the vertical turbulent fluxes are taken into account while all horizontal gradients and turbulent fluxes are set to zero in Eqs. (1)–(4). The

mixing length is parameterized, following Bougeault and Lacarrère (1989), as the maximum vertical displacement allowed for a parcel characterized by a TKE value to travel upward (l_{up}) or downward (l_{down}) before being stopped by buoyancy effects. The mixing length is defined by

$$L = \left[\frac{(l_{up})^{-2/3} + (l_{down})^{-2/3}}{2} \right]^{-3/2}, \quad (6)$$

with the maximum vertical displacements l_{up} and l_{down} given by

$$\int_{z}^{z+l_{up}} \frac{g}{\theta_{vref}} [\theta_v(z') - \theta_v(z)]\, dz' = e(z), \quad (7)$$

$$\int_{z-l_{down}}^{z} \frac{g}{\theta_{vref}} [\theta_v(z) - \theta_v(z')]\, dz' = e(z). \quad (8)$$

The mixing length at any level is therefore determined not only by the stability at this level, but by the effect of remote stability. In that sense, it is a nonlocal length. In summary, the 1D and 3D modes differ on the treatment of mixing length, the neglect of horizontal gradients in parameterizing the various Reynolds stress terms [Eqs. (1)–(4)], and the neglect of horizontal subgrid mixing.

During the campaign, the model was run with the turbulence scheme set in 1D mode as the 2-km horizontal grid spacing was too coarse to represent large horizontal gradients. This assumption, which is generally correct within the atmospheric boundary layer, is, however, questionable within convective clouds and their close environment. This motivated the sensitivity tests performed with the turbulence scheme in the 3D mode. It is also worth mentioning that the subgrid shallow convection of Pergaud et al. (2009) was used for representing thermals (nonlocal turbulence) in the boundary layer. As shown by Honnert et al. (2011), running the Méso-NH model at kilometer scale without the subgrid shallow convection would result in too strong resolved motions because of lack of mixing by the turbulence scheme.

b. *Evaluation approach*

The MSG images and the constant-altitude plan position indicators (CAPPIs) of the S-band radar (10-cm wavelength) at Canguçu, Brazil, were used. The MSG images employed in the present study were at the 10.8-μm brightness temperature (Tir), as these are the images mainly affected by the cloud-top emission. The radar data were from 2- to 15-km height, covering a 250-km radius, with 1-km spatial resolution. The radar was the most suitable instrument for comparisons with rainfall simulations because of the very similar resolution of its measurements compared to the inner model nest and its close relationship to the rainfall field. However, radar data present several nonprecipitation echoes (clutter or other associated errors) that are very difficult to filter out automatically. To avoid this echo-induced noise, we used only rainfall cell pixels having reflectivity values larger than 20 dBZ. The region covered by the radar was only part of the whole simulated region (around 25% of the area, see Fig. 1) employed in the comparison with satellite images.

Five "golden" cases were chosen as the most important convective systems crossing the field campaign experiment. All were associated with a large-scale cloud organization forced by cold frontal systems penetrating into South America. The mesoscale systems formed during these days were generally very well organized. The golden days studied were Julian days 327, 333, 335, 338, and 345. For each case, an hourly comparison was performed with satellite data and, for some days, with radar (only a few days had a complete data record). Each golden case consisted of a 36-h simulation starting from 1200 UTC on the considered Julian day until 0000 UTC two days after. When a case study is mentioned as a specific Julian day, it corresponds to 36 satellite or radar images and model simulations, one each hour, projected over the 2-km horizontal grid spacing grid model for satellite or 1-km grid resolution grid radar for radar comparisons. The comparison using the radar horizontal field, CAPPI at 2-km height, was used to approximately represent the precipitation field. For the evaluation using three-dimensional fields, observations were computed using 1-km radar vertical resolution. A spinup time of 5 h was considered in the simulations of satellite images. Therefore, the comparison with observation was done over the last 31 h of simulation, from 1700 UTC on the considered Julian day, which corresponds to 1400 local time (LT) when deep convection is starting to develop.

3. Impact of the turbulence scheme in 1D and 3D mode for a case study

a. *Comparison with satellite observation*

Figure 1 shows the Tir from MSG and the Méso-NH simulations for Julian day 335 (30 November) with lead times from 8 to 32 h, every 12 h. The case was characterized by the passage of a cold front that traveled northeastward over the simulation domain from the southwestern corner. Before the arrival of the cold front, the MSG observation showed large clear-sky Tir values at 2000 UTC 30 November (Fig. 1a). At that time, 1700 LT,

the two simulations overestimated the cloud cover by already producing high-level clouds, especially the simulation with 1D turbulence (Figs. 1d,g). At 0800 UTC 1 December (0500 LT), the cold front lay along a northwest–southeast line over Paraguay, northern Argentina, and the Brazil–Uruguay border. Ahead of this front, cold cloud tops were embedded in stratiform clouds surrounded by mid- and low-level clouds (Fig. 1b). The simulations showed a cloud organization ahead of the cold front similar to what was observed, but with more mid- and low-level clouds (Figs. 1e,h). Moreover, thunderstorms appeared as several compact cloud systems while they were more scattered in the simulations. The simulation with 3D turbulence performed better in the cloud organization than the one with 1D turbulence, but lacked the system standing over northern Argentina. At 2000 UTC 1 December, the cloud systems were observed in the northern and eastern boundaries of the simulation domain (Fig. 1c). Again, the simulation with 1D turbulence produced too many cloud systems (Fig. 1f), while the simulation with 3D turbulence forecasted a cloud organization that matched the observation rather well (Fig. 1i).

To further assess the effect of the turbulence scheme, we used the equitable threat score (ETS) to quantify the ability of the model to forecast a cloud event at the right place. The ETS measures the fraction of correct forecasts after eliminating those that would occur simply due to chance. Values of ETS are, by definition, less than 1, with one being the perfect score and zero meaning that all successful forecasts can be attributed to chance. Categorical scores such as ETS are widely used to compare models or verify the impact of a change in model parameterization. We used the ETS to compare the occurrence of high clouds using a Tir threshold of 260 K simulated by Méso-NH and observed by MSG, following the methodology employed by Söhne et al. (2008). Figure 2 shows the ETS for Julian day 335 for the two simulations. Up to 11-h lead time, the two simulations present similar ETS while overestimating the cloud fraction from a 6-h lead time. Thereafter, the simulation with 3D turbulence is by far the best and its score tends to increase with time, up to a maximum of 0.45. Between the 32- and 34-h lead time, its score is significantly higher as the simulation with 1D turbulence. Figure 2 also shows the 260-K threshold cloud fraction observed by satellite and forecasted. Note the better agreement of the simulation with 3D turbulence with the satellite observation after the 6-h lead time.

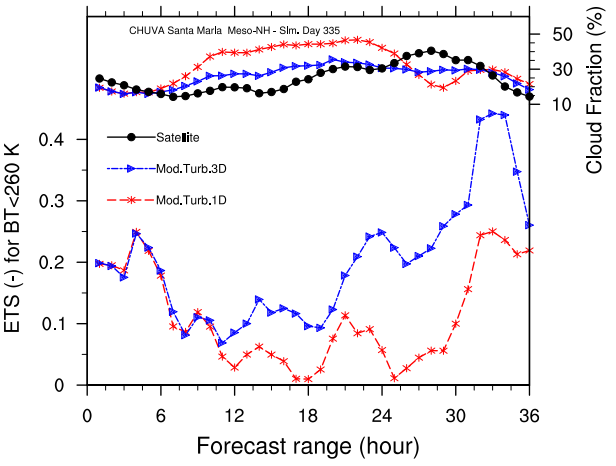

FIG. 2. ETS for the occurrence of high clouds using a brightness temperature threshold of 260 K, simulated by Méso-NH with 1D and 3D turbulence during the 36-h period from 1200 UTC of Julian day 335. The fractional cloud cover of high clouds is also shown for the MSG observation and the simulations.

b. Impact on turbulent mixing inside clouds

The difference between the two simulations was solely due to the formulation of the subgrid turbulence scheme, which differs between the 1D and 3D mode. A major difference in these two modes of the turbulence scheme is the calculation of the mixing length. As the subgrid turbulent kinetic energy in the free troposphere is produced mostly where deep convection occurs, the impact of the turbulent mixing is analyzed inside clouds in the following.

Figure 3a shows the 25th, 50th, and 75th percentiles of the mixing length hourly averaged profiles inside clouds (defined as grid points with mixing ratio larger than 0.01 g kg^{-1}). For the 1D mode, the mixing length increases with the subgrid TKE following the parameterization of Bougeault and Lacarrère (1989). Because the value of the subgrid TKE inside clouds, mainly above the boundary layer, is small, it resulted in a median value of the in-cloud mixing length around 15 m that did not change much with lead time. For the 3D mode, the mixing length equals the grid size limited by the thermal stability. This allowed much larger values of the mixing length inside clouds. Individual values up to 1.3 km were found in unstable cloudy areas (not shown). Although its median value was lower than that of the 1D mode above 4-km altitude, the 75th percentile value inside clouds was much larger in the lower part of the troposphere than that of the 1D mode, with a value reaching 40 m at 3.5-km altitude (i.e., just below the freezing level located around 4 km).

By construction, the larger mixing length for 3D turbulence than for 1D turbulence found inside clouds below the freezing level increases the subgrid TKE, which enhances the mixing there. The net effect of mixing (including subgrid mixing and other processes) is

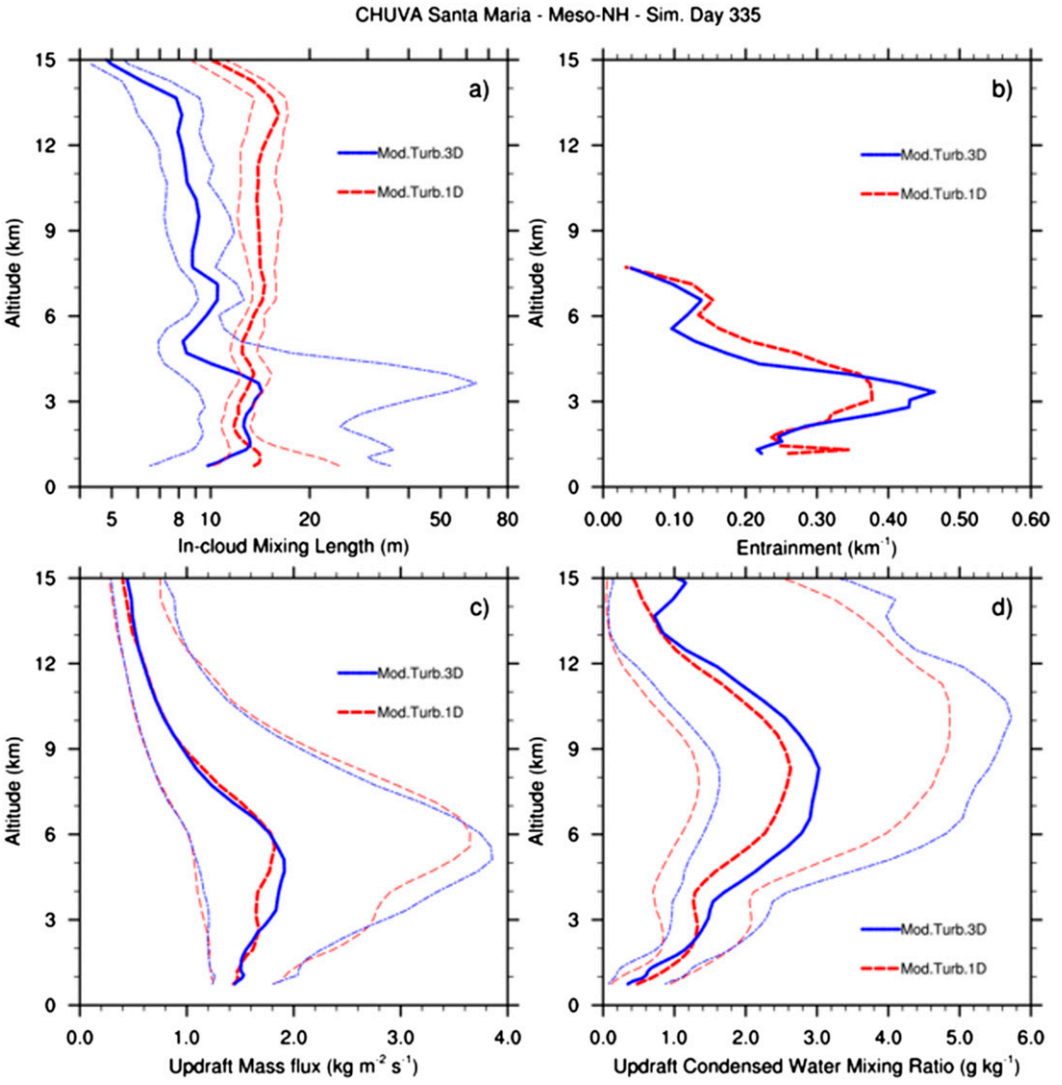

FIG. 3. Vertical profiles of (a) mixing length, (b) entrainment, (c) updraft mass flux, and (d) updraft condensed water mixing ratio simulated by Méso-NH with 1D and 3D turbulence for Julian day 335. Thick lines represent the median values while thin lines in (a),(c), and (d) represent the 25th and 75th percentiles.

illustrated with the entrainment computed for cloudy updraft cores. The latter are defined as grid points with vertical wind speed higher than 1 m s^{-1} and cloud mixing ratio larger than 0.01 g kg^{-1}. Following Del Genio and Wu (2010), the calculation of the entrainment ε used the standard bulk plume model for the frozen moist static energy h:

$$\frac{\partial h_u}{\partial z} = \varepsilon(h_e - h_u), \tag{9}$$

where z is height and the subscripts u and e refer to the frozen moist static energy for the cloudy updraft and the environment, respectively. The frozen moist static energy is conserved below levels at which ice precipitation forms. Therefore, entrainment was calculated up to 8-km altitude. As expected from the mixing length found inside clouds, the simulation with 3D turbulence showed a much larger entrainment at 3.5-km altitude than the one with 1D turbulence (Fig. 3b). The larger entrainment produced by 3D turbulence could explain the decrease in the number of cloud systems seen in Tir images (Fig. 1). Conversely, the lower mixing length for the 3D mode found inside clouds above 4–5 km contributes to an entrainment of the updraft cores lower than for the 1D mode in the higher levels. However, the relationship between subgrid-scale mixing and entrainment is complicated. Several other processes also impact the model cloud size distribution. The difficulty

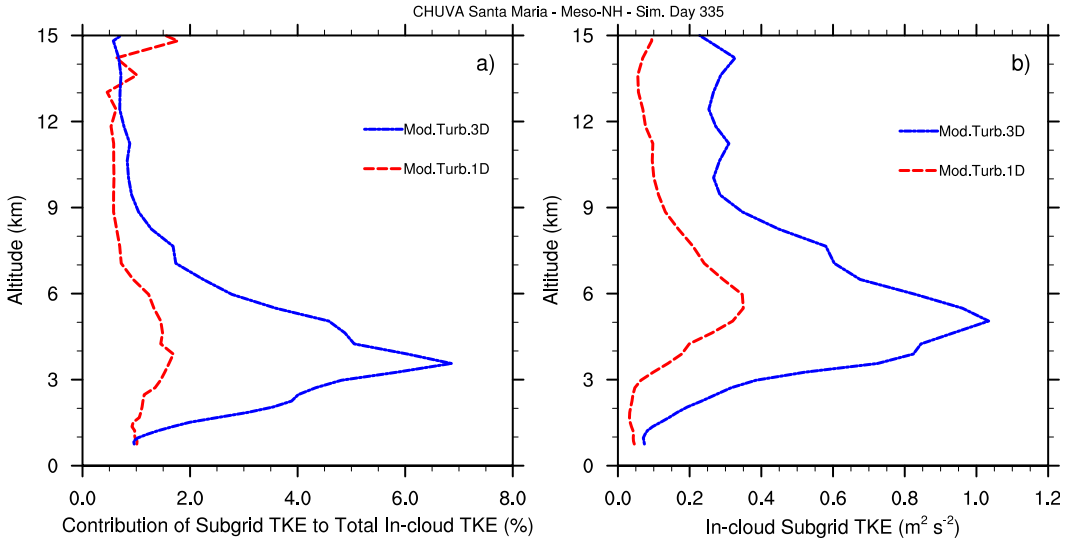

FIG. 4. Vertical profiles of (a) contribution of TKE to the total in-cloud TKE and (b) subgrid in-cloud TKE simulated by Méso-NH with 1D and 3D turbulence for Julian day 335.

of the model to simulate the updraft size distribution with a 2-km grid spacing adds to this complexity, because the overall entrainment for cloudy updraft cores is a combination of resolved-scale motions, subgrid mixing, and numerical diffusion.

The change in the mixing length impacted the mass flux of the cloudy updraft cores (Fig. 3c). The latter was calculated as the air density multiplied by the vertical velocity at every grid point with a vertical wind speed higher than $1\,\mathrm{m\,s^{-1}}$ and a cloud mixing ratio larger than $0.01\,\mathrm{g\,kg^{-1}}$. The largest impact was found at the altitude where the difference in the mixing length was the greatest. At 3.5-km altitude, the mass flux for 1D turbulence was smaller than the one for 3D turbulence. The lower mixing between the cloudy updrafts and their environment could lead to more buoyancy than were the parcels with a larger mixing length and therefore keep more updrafts alive, but with weaker mass flux than for 3D turbulence. As a result, the condensed water within the updraft cores showed a smaller mixing ratio in 1D mode than in 3D mode above 3-km altitude whatever the percentile (Fig. 3d). The results are consistent with those obtained by Verrelle et al. (2015) using the Méso-NH model for an idealized supercell. Their 2-km grid spacing simulation with 3D turbulence has significantly larger area of updraft than their 2-km grid spacing simulation with 1D turbulence. It induces more mixing and enhances the microphysical processes compared to the simulation with 1D turbulence, producing larger amounts of cloud cover and precipitation. Verrelle et al. (2015) stated that the difference between simulations with 1D and 3D turbulence becomes perceptible at 2-km grid spacing, showing the importance of horizontal turbulent fluxes. Fiori et al. (2010) simulated a supercell using different resolutions and turbulence closures. They observed a very different behavior for different closures and resolutions and concluded that more simplified turbulence closures such as 1D yield substantially worse results than the simulations using large-eddy simulation.

The impact of subgrid turbulence parameterization was further addressed by analyzing the total turbulence inside clouds. The grid-scale TKE was calculated from the deviation of the grid-scale kinetic energy with respect to the mean kinetic energy calculated within clouds (i.e., for grid points with cloud mixing ratio larger than $0.01\,\mathrm{g\,kg^{-1}}$). Figure 4 shows the contribution of the subgrid turbulence to the total TKE and the subgrid TKE averaged inside clouds and for Julian day 335. The mean subgrid TKE reached values up to 0.3 and $1.0\,\mathrm{m^2\,s^{-2}}$ with 1D and 3D turbulence, respectively. Its contribution to the total TKE was thus rather small, up to a maximum of about 7% with 3D turbulence and 1.5% with 1D turbulence. Such a small amount was also found by Verrelle et al. (2015) for an idealized supercell. This is partly due to the way the grid-scale TKE was calculated, which includes a contribution from the larger scale of the updrafts. As expected, the maximum for 3D turbulence was located at the altitude where the maximum of the mixing length was found. The weaker subgrid TKE found inside clouds for the 1D mode can be explained partly by the in-cloud mixing length being smaller than for the 3D mode. It is also due to the weak vertical gradient of the prognostic variables compared to their horizontal counterpart, particularly at cloud boundaries. Indeed, the calculation of the subgrid TKE is

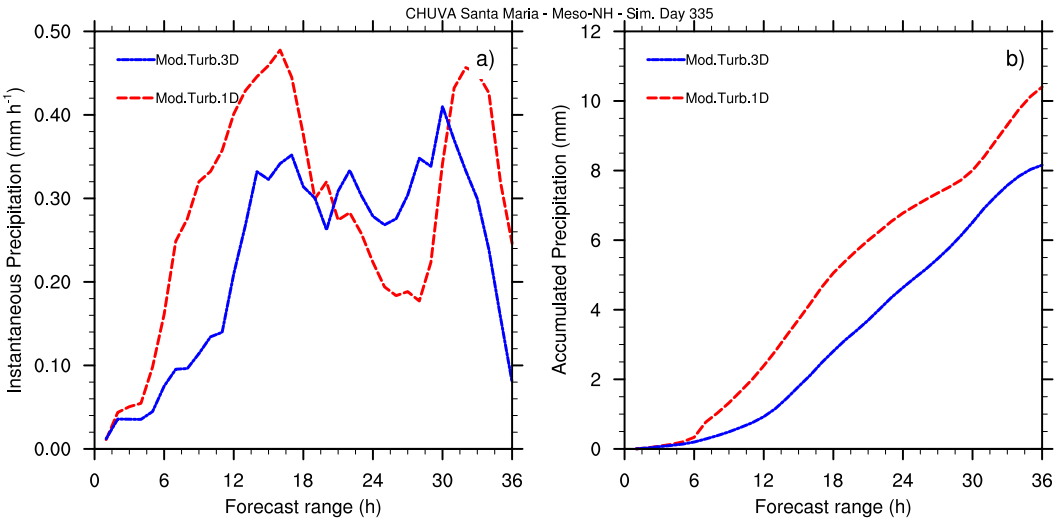

FIG. 5. (a) Instantaneous and (b) accumulated precipitation simulated by Méso-NH with 1D and 3D turbulence for Julian day 335.

based on the resolved gradients of wind, temperature, and moisture, directly [Eq. (1)] and indirectly by the diagnostic equations of fluxes [Eqs. (2), (3), and (4)]. Their horizontal gradients also contribute to the horizontal subgrid-scale mixing. Therefore, taking them into account increases the subgrid TKE as shown for the 3D mode.

The impact of the turbulent mixing inside clouds was finally assessed on the surface precipitation. The instantaneous precipitation increased much more rapidly with 1D turbulence than with 3D turbulence (Fig. 5a). This result is consistent with the earlier formation of deep convective clouds shown in the Tir images (Figs. 1d,g). Later on (from the 20-h lead time), more instantaneous precipitation was produced in the simulation with 3D turbulence. This was due to a more organized cloud system as shown at 0800 UTC 1 December (Figs. 1e,f). As a result, the accumulated precipitation (Fig. 5b) was larger for the simulation with 1D turbulence than for the one with 3D turbulence. In that case, the increase was rather large, around 20% and results on precipitation for the other golden days showed a smaller change, around 10%. This change was generally, but not systematically, an increase in precipitation for 1D turbulence. This result underlines the indirect relationship between the turbulence mode and the resulting precipitation.

4. Statistical impact of the turbulence scheme in 1D and 3D mode

a. Overall performance of the Méso-NH simulations

The Méso-NH simulations with 1D and 3D turbulence are now compared against observations from the statistical point of view. This step in comparing satellite image and numerical model simulation consisted in utilizing the histogram technique, traditionally used in studies comparing model and satellite data. For example, Chaboureau et al. (2008) employed this technique for the evaluation of Méso-NH cloud fields and the retrieval of hydrometeor characteristics using the model outputs. Figure 6 shows the Tir histogram for the MSG observations and the two sets of Méso-NH simulations for the 31 images of each Julian day for all 5 golden days. The three histograms compare well, with a peak for high Tir associated with clear-sky and low-level clouds, a nearly constant frequency between 260 and 230 K, and a fast decrease in the Tir population for Tir less than 230 K. The largest discrepancies in the simulations were observed for (i) the Tir range of clear-sky–low-level clouds larger in the simulation and (ii) the smaller frequency of low Tir between 260 and 200 K, partly as consequence of the relatively larger proportion of clear sky pixels. The population of very cold tops, with Tir lower than 200 K, was very similar in the observations and the simulations. These results indicate that the Méso-NH simulations produce more clear-sky–low-level clouds, a smaller population of stratiform–convective clouds, and a nearly similar amount of deep convective clouds. This behavior was reasonably similar from day to day (not shown) and was not very sensitive to the turbulence mode used by the model.

b. Space–time organization of clouds

The novelty of the evaluation approach, used in the observation space, was to assess the cloud organization, a property that cannot be evaluated with a Tir histogram.

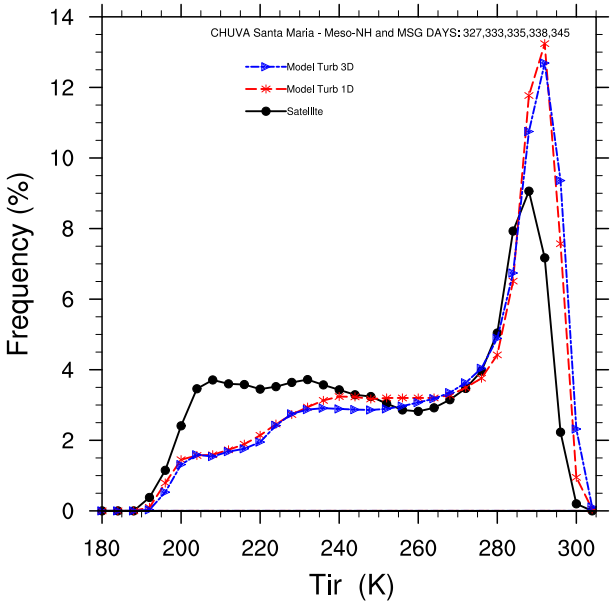

FIG. 6. Tir histogram of the 5 golden days simulations obtained from the observations and the simulations with 1D and 3D turbulence.

We checked whether the simulated cloud and rain fields described the same organization as observed by MSG and the S-band radar, respectively. Cloud organization was defined as clusters of pixels with Tir lower than 235 K. Machado et al. (1998) discussed the use of this threshold to represent the organization of convective clouds into clusters using satellite images. The clusters of 235-K pixels were tracked using the Forecast and Tracking the evolution of Cloud Clusters (Fortracc) technique, described by Vila et al. (2008). Fortracc is an algorithm that tracks the MCS radiative and morphological properties, using infrared satellite imagery or radar in a regular grid. The main components of this software are the following: a cloud cluster detection method based on a size and temperature threshold; a statistical module to determine the morphological and radiative parameters of each convective system; a tracking technique based on overlapping of convective system areas in successive images; and a forecast module based on the evolution in previous time steps. This last module was not employed in this study. The minimum size tracked using satellite data was 10 pixels, which corresponds to an effective radius (the radius of a sphere having the same area as the cloud or rain cell) of around 3.5 km. No significant differences in the overall result were obtained when employing different thresholds as shown by Machado et al. (1998). The analysis of radar rainfall cell size was applied using a 20-dBZ threshold following Machado et al. (2002). Considering a Marshall–Palmer distribution, a reflectivity value of 20 dBZ corresponds to a rain rate of 1 mm h^{-1}.

Figure 7a shows the cloud size distributions observed by MSG and simulated by Méso-NH for the 5 golden days. The Méso-NH cloud field simulated with 1D turbulence had nearly twice as many small cloud systems as were actually observed. This difference in cloud system numbers decreased as the cloud system size increased. It resulted in a similar number of systems with effective radius above 100 km. For the largest convective systems (i.e., beyond an effective radius of 300 km), the model with 1D and 3D turbulence simulated fewer systems than were observed. It should be noted that, although the difference in the number of the largest cloud systems was very small, the latter can cover some very large areas. For instance, one cloud system with a 300-km effective radius covers the same area as 900 cloud systems with a 10-km effective radius. The simulations with 3D turbulence also showed a larger number of small cells than observed by satellite, but this number was reduced by 20% compared to the simulations with 1D turbulence. Similar results of a reduced number of small cells with 3D turbulence were obtained for every golden day.

Figure 7b shows the life cycle duration of the convective systems. The simulations with 1D turbulence present many more short-lived systems than were observed. The simulations with 3D turbulence show a slightly smaller number of short-lived cloud cells than the simulations with 1D turbulence. The difference is very clear for cloud systems with a life cycle shorter than 4 h. As the life cycle duration increases, the difference decreases. From 6 h, simulations and observations show nearly the same number of long-lived cloud systems. Beyond 10 h, satellite observation shows longer life cycles than the two sets of simulations.

The strong difference in the space–time organization of clouds between simulations and observations contrasts with the relative agreement obtained with the Tir histogram for which the 1D and 3D simulations produce nearly identical results. To better understand this deficiency in the organization, Fig. 8 shows the averaged Tir histograms for the small (smaller than 50-km effective radius) and large (larger than 150-km effective radius) cloud systems. As a cloud system is defined as a cluster of Tir lower than 235 K, its average Tir is thus below 235 K. Nearly 80% of the observed small cloud systems had average Tir higher than 230 K and very few had Tir lower than 220 K (Fig. 8a). This contrasts with the larger number of small cloud systems with low Tir in the simulations. The comparison for the large cloud systems presents a systematic, albeit less remarkable, discrepancy. Large systems in the observations showed higher average cloud-top height (lower Tir) than in the simulations (Fig. 8b).

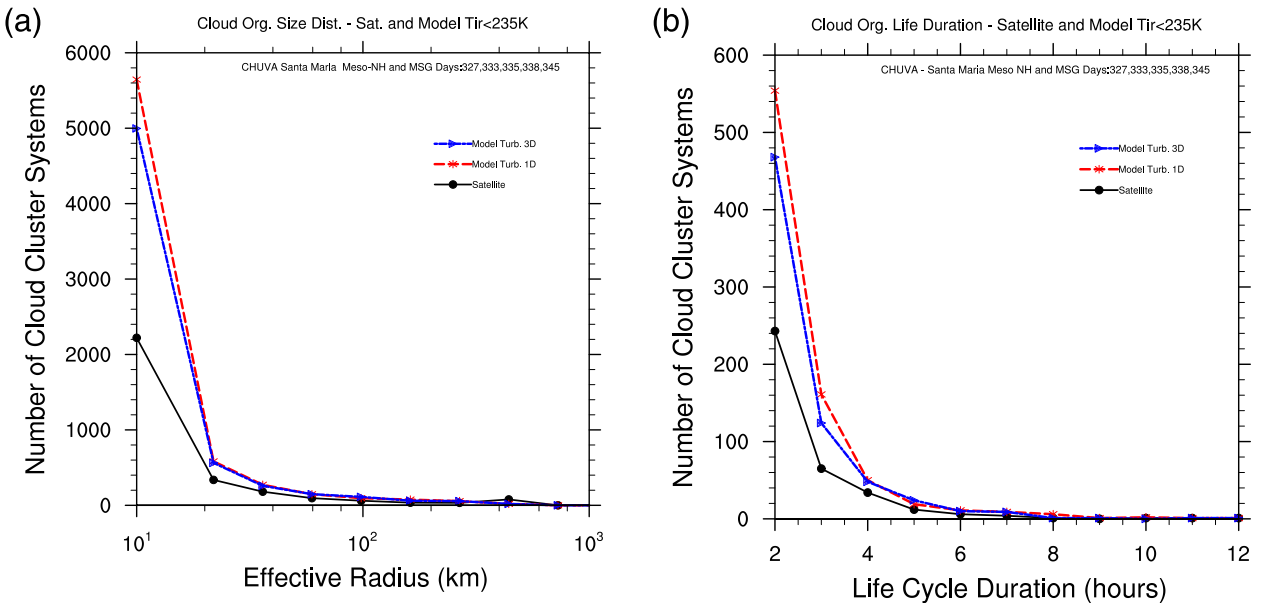

FIG. 7. Organization of clouds (Tir < 235 K) observed by MSG and simulated by Méso-NH with 1D and 3D turbulence for the 5 golden days simulations. (a) Size distribution and (b) life cycle duration.

These results indicate that the simulations with 1D turbulence showed a larger number of small systems with deeper cloud top than was observed and a smaller number of large systems, less deep than observed. Simulations with 3D turbulence also showed similar errors, but with somewhat a reduced magnitude compared to those with 1D turbulence. One possible reason for the too large number of too deep, small clouds is a relatively smaller entrainment rate than what could be expected for an entrainment calculated as an inverse function of radius. Such sensitivity of cloud size to entrainment is well known; Simpson (1971) proposed a parameterization of the entrainment rate with inverse dependence on the tower radius. It is therefore expected to have a larger

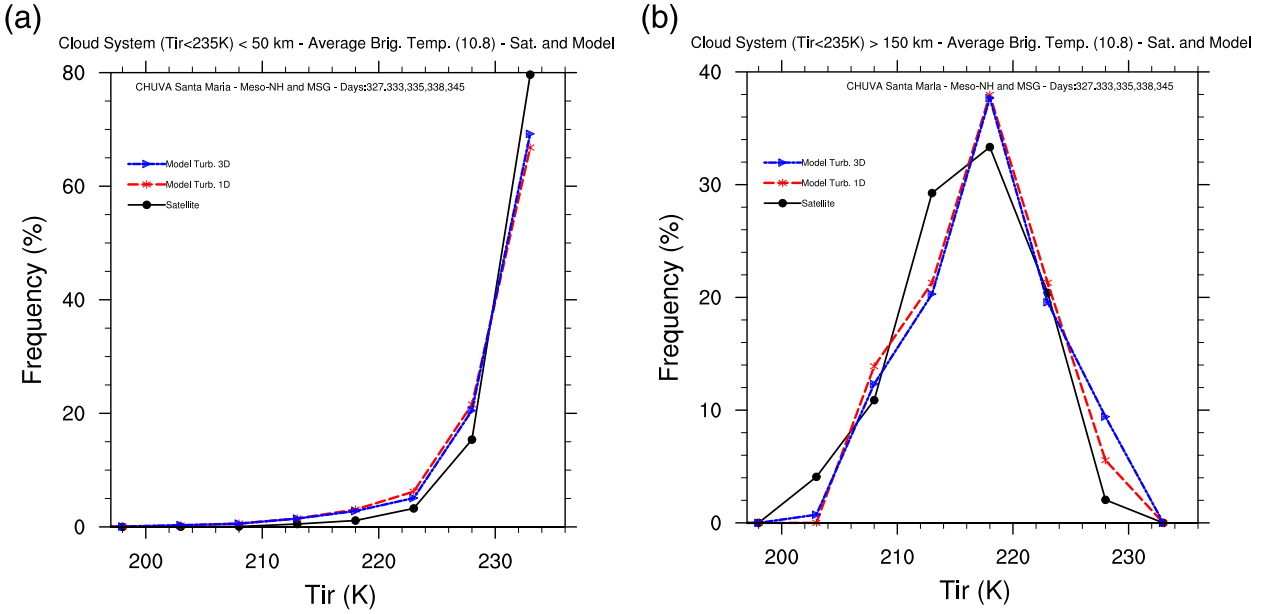

FIG. 8. Tir histogram of cloud cells (Tir < 235 K) with effective radius (a) smaller than 50 km and (b) larger than 150 km observed by MSG and simulated by Méso-NH with 1D and 3D turbulence for the 5 golden days simulations.

entrainment for small clouds than for large ones. It seems, however, that the entrainment still needs to be larger than the one produced by the model. This may be explained by two considerations. First, the cloud size differs from the updraft size, especially for larger cloud systems with large anvil shields. Second, convective updrafts are by their nature turbulent and individual updraft cores are under-resolved with a 2-km grid spacing. Hence, they should be larger, leading to a smaller entrainment than expected. An underestimation of the mixing between convective cloud updrafts and their environment can lead to cloud fields as seen in the simulations. Jensen and Del Genio (2006) examined the environmental factors that could determine the depth of convective clouds and the environmental parameters that could be related to the entrainment rate. They found that buoyancy close to the surface, the major source of kinetic energy, was the main factor responsible for the variability in entrainment rate. However, as their study was limited to the development of cumulus congestus clouds, they could not classify the effect of this variability for a large population of clouds, which should also experience different degrees of entrainment according to their size. Bryan et al. (2003) discussed the appropriate spatial resolution for the simulation of deep moist convection. They observed that, with the increase of resolution, a simulation is significantly more turbulent and consequently entrainment in updrafts is better resolved. They concluded that the 1-km simulations do not adequately resolve turbulent fluxes of total water. A similar result was presented by Bryan and Morrison (2012). The latter observed a broader spectrum of updraft sizes in simulations with high resolution than those with low resolution. As the spatial resolution increases, the turbulence is better described and the updrafts well represented. In the present simulations with 2-km grid spacing, the changes in the turbulence parameterization can help to improve the turbulence features and consequently the entrainment. As stated in our results, cloud and rain cell size are smaller than observed but individual updraft cores are under resolved and hence too large, leading to a smaller entrainment. This could be the reason for the differences in cloud and rain size distribution and cloud top between simulations and observations. Using the 3D turbulence, which results in an enhanced mixing, can improve the size distribution and partially compensate the insufficient resolution of thunderstorm cells.

Last, the simulations produced a lower number of large systems than was observed. The mechanisms leading to large systems are much more complex than for the small systems because of the mesoscale dynamics. This partly explains the small sensitivity of the number of large systems to the turbulence parameterization. The underestimated number of large systems could also be related to some model limitations in simulating large convective systems with large stratiform cloud decks.

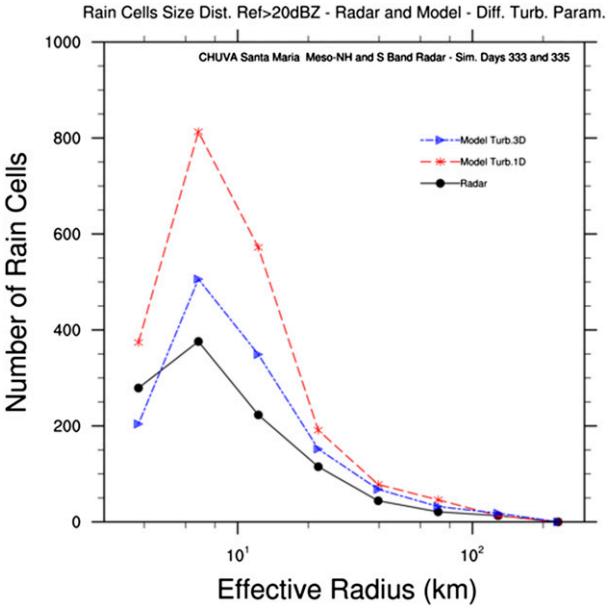

FIG. 9. Organization of rain cells (reflectivity larger than 20 dBZ) observed by the S-band radar and simulated by Méso-NH with 1D and 3D turbulence for Julian days 333 and 335 simulations.

c. *Space–time organization of rainfall cells*

We now verify the impact of 1D and 3D turbulence on the organization of rainfall cells for Julian days 333 and 335. These days were chosen because the 36-h sequence from the simulated day at 1200 UTC was fully covered by the S-band radar at least once per hour. Even an hour is too long an interval to be used for tracking rainfall cells (which have much shorter lifetimes than the cloud systems) but the size description is independent of the time interval. Figure 9 shows the size distribution of the rainfall cells for observations and simulations using 1D and 3D turbulence. It shows the larger number of rain cells simulated by 1D turbulence than the rainfall field observed by the radar, and the considerably lower number of small rainfall cells using 3D turbulence. This result shows that, whether we consider clouds or rainfall, the model simulated more small individual clouds and rain cells than observed. The 3D turbulence improved the results by reducing the number of small clouds and especially rain cells.

The turbulence scheme in 3D mode gave a reasonable improvement in the representation of the cloud and rainfall spatial organization. Figure 10 shows the

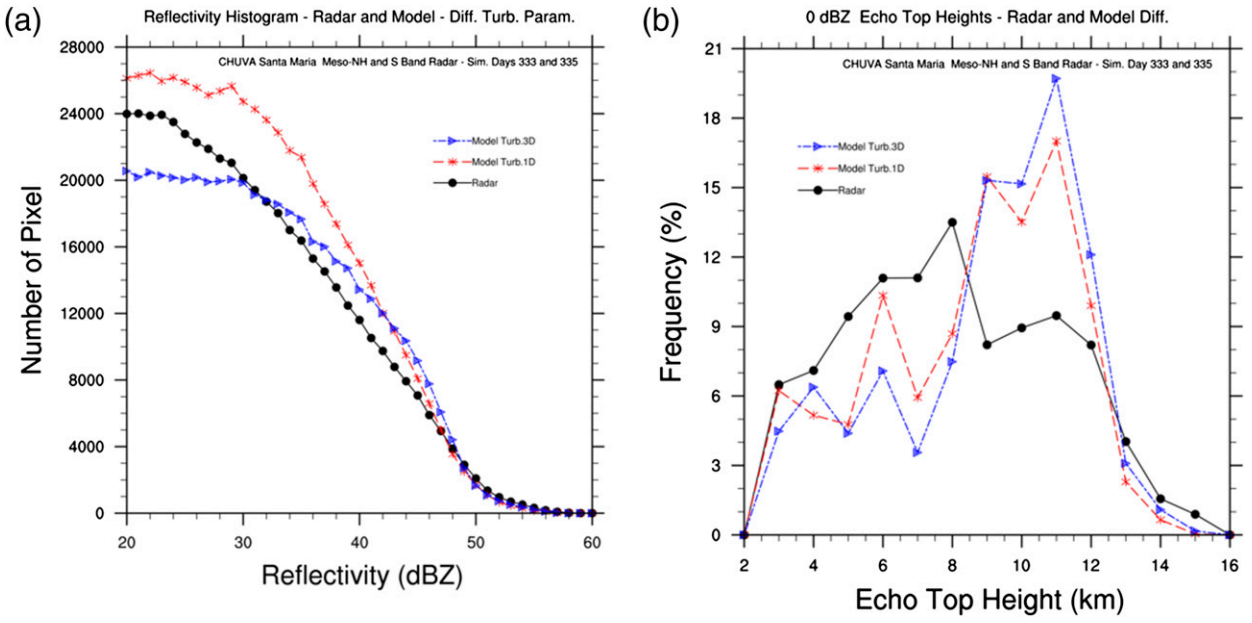

FIG. 10. Reflectivity from S-band radar and Méso-NH simulations with 1D and 3D turbulence for Julian days 333 and 335 simulations. (a) Histogram of reflectivity at 2-km altitude and (b) normalized histogram of echo cloud-top height using the 0-dBZ threshold.

histogram for the reflectivity at 2 km and the normalized histogram for the 0-dBZ echo cloud-top height distribution. Note the higher number of reflectivities between 20 and about 46 dBZ compared to observations using 1D turbulence (Fig. 10a). The use of 3D turbulence has the effect of reducing this population although the number of reflectivity values between 32 and 46 dBZ is also greater than observed. Whatever the turbulence mode, the relative frequency of the cloud-top echo (raindrop) distribution is not very well represented by the model (Fig. 10b). The simulations reduce the relative population of cloud tops between 4 and 8 km and the very high cloud tops, typically associated with intense deep convection and increase, relatively, the population of cloud tops between 8 and 12 km. Although, both histograms are very similar, the simulations with 3D turbulence present a slightly smaller frequency of clouds with cloud tops below 9 km and a slightly larger frequency of high clouds than 1D simulations. This is expected because of the larger entrainment reducing the number of small cells, while the number of high clouds does not change much.

The turbulent scheme in 3D mode takes the horizontal turbulent fluxes into account, which are neglected in the 1D mode. However, these two turbulent modes were used with different mixing length parameterizations: the 1D mode used the Bougeault and Lacarrère (1989) mixing length while the 3D mode took the Deardorff mixing length. The differences seen above are a combination of these two effects (i.e., the change in the mixing length parameterization and the additional horizontal turbulent fluxes that contribute to both the calculation of TKE and the horizontal subgrid-scale mixing). To test the impact of these two effects, additional simulations were run using the 1D mode with the Deardorff mixing length and the 3D mode with the Bougeault and Lacarrère (1989) mixing length (not shown). Whatever the mixing length parameterization, the simulations with 1D turbulence did not show significant differences in cloud organization. In the simulations with 3D turbulence, the cloud organization differed according to the mixing length parameterization. This suggests that the larger horizontal potential temperature gradient at the cloud boundaries had a significant impact in the simulations. Because of the importance of the mixing length in 3D turbulence, this effect was investigated specifically inside clouds.

5. Sensitivity to mixing length inside clouds

The turbulence scheme in 3D mode has considerable impact in the space–time organization of clouds and rainfall. Now, the effect of the mixing length that acts directly in the turbulence scheme needs to be evaluated. Emanuel (1994) shows that the interface between cloud and environment undergoes small-scale instabilities that enhance the mixing. The mixing length may be too small to take such an effect into account where the gradients

of prognostic variables are insufficiently resolved as well the updrafts with the 2-km grid spacing. Here we tested the effect of changing the mixing length inside clouds only.

As the effect of turbulence has impact in the cloud size distribution as shown in the previous results, we investigated the effect of the in-cloud mixing length multiplied by a constant coefficient α. To conduct this analysis, we tested the effect of the in-cloud mixing length scaled by a factor of 2 (i.e., we multiplied the mixing length inside the clouds by $\alpha = 0.5$ and by $\alpha = 2$, forcing small and large entrainment, respectively). Figure 11 shows the cloud size distribution during the simulation for Julian day 335. The effect of the scale factor is very significant. It increases the number of small systems when $\alpha = 0.5$, while drastically reducing the number of cloud systems when $\alpha = 2.0$. This result shows the effect of the change of in-cloud mixing length for the simulations and its impact with respect to the cloud size. As discussed before, the inability of the model to reproduce a broad spectrum of updrafts with a 2-km grid spacing can lead to a small mixing in the cloud; however, the increase in the mixing by increasing α can compensate this feature. Based on the previous results, we can suppose that the modulation of this factor could depend on the size of the updraft (here we consider that size of the updraft is proportional to the size of the cloud system). For small updrafts, the factor applied to the mixing length should be very high. The very high values employed here were intended to demonstrate the effect of this scale factor on the mixing length inside clouds. More adequate values, certainly closer to a scale factor of 1, should be tested to obtain a more realistic cloud organization.

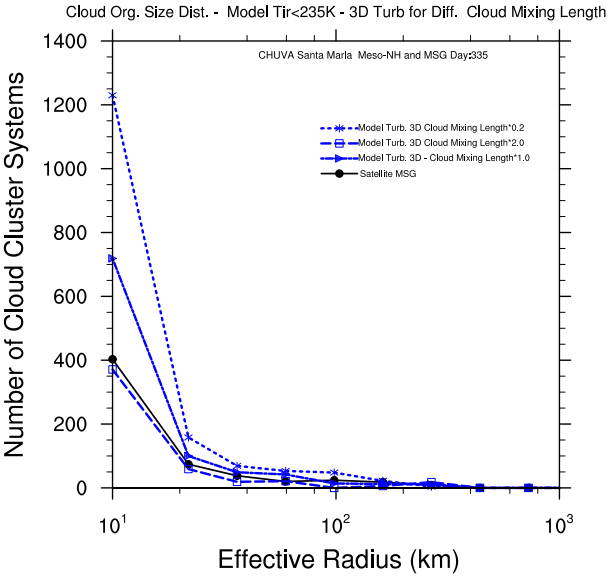

FIG. 11. Organization of clouds (Tir < 235K) observed by MSG and simulated by Méso-NH with 3D turbulence for cloud mixing length multiplied by 0.5, 1.0, and 2.0, for simulation of Julian day 335.

6. Conclusions

This study has presented an innovative procedure for evaluating cloud organization in space and time in cloud-resolving models and assessing their representation of turbulence. Comparisons were performed with satellite and radar data to study the radiative properties and the morphology of the cloud organization. The analysis employed used the data collected during the CHUVA-SUL campaign, MSG images, and Méso-NH simulations. Five main events of synoptic-scale forcing producing mesoscale convective cloud organization were analyzed. Overall, the total histogram distribution of Tir was quite similar between simulation and observation for the five golden cases, although the model generally produced more clear-sky and low-level clouds, and fewer midlevel to deep clouds than were actually observed. Nevertheless, the cloud and rain cell organization in space and time among the different simulations was very different.

The simulations with 1D turbulence produced a larger number of small, tall convective systems than observed. This was true for the cloud organization compared to satellite data and for the rain cells compared to the radar data. The life cycle duration simulated with 1D turbulence showed too large a population of short-lived cloud cells compared to the situation observed by MSG. The Tir histogram, for small cloud organization only, showed deeper simulated clouds than observed. Conversely, the simulated large cloud clusters presented cloud tops that were statistically warmer than the observations. These results, for simulations with 1D turbulence, demonstrated that the model produced a larger number of small, deep cells than observed and nearly the same number of large cells, but which were shallower than in the observations. One possible explanation for these discrepancies is that the entrainment produced by the simulations with 1D turbulence should be larger, mainly for small cloud systems. This leads to too many small, deep cells. The turbulence scheme in the 1D mode seems to lack accurate descriptions of the turbulent kinetic energy and the mixing process. When we look at the general skill score, the simulation with 3D turbulence is much better than that with 1D turbulence.

The turbulence scheme in 3D mode with the Deardorff mixing length was tested to check its effect on cloud organization. It resulted in a reduced number of

small cloud systems and rain cells, presenting a distribution somewhat closer to what was observed, but still with more small cells and a larger population of short-lived cells than observed.

The 3D turbulence yielded much larger values of the in-cloud mixing length, mainly in the lower part of the troposphere, just below the freezing level, than did the 1D turbulence. As a consequence, the simulations with 3D turbulence showed a much larger entrainment at around 4-km altitude than the ones with 1D turbulence. The change in the in-cloud mixing length also impacted the mass flux and the condensed water within the updraft cores around the freezing level. The latter were smaller for 1D turbulence than those for 3D turbulence. As a result of this small in-cloud mixing length in 1D turbulence, the instantaneous precipitation increased much more rapidly with 1D turbulence than with 3D turbulence. Of course this is a very complex interaction and others factors can also contribute to this effect as, for instance, the sharp horizontal gradients of temperature and moisture at the boundaries of thunderstorms.

A comparison of the reflectivity histogram and cloud-top distribution shows simulations with 3D turbulence producing fewer cases of cloud tops below 10-km height and reflectivity smaller than 40 dBZ than the ones with 1D turbulence. The deepest cells, having very high reflectivity and tops higher than 12 km, are more frequent in the simulations with 3D turbulence than with 1D turbulence. Results comparing simulations and radar were similar to those obtained by satellite. The simulations with 3D turbulence produced somewhat fewer small rain cells and these cells were less deep than those produced by 1D turbulence. For the large rain cells, associated with the high reflectivity and cloud-top height, the simulations with 3D turbulence produced deeper rain cells with higher reflectivities than those produced by 1D turbulence.

The simulations with 3D turbulence mode were highly sensitive to the mixing length parameterization. Therefore, a sensitivity test was carried out by increasing and decreasing the mixing length inside clouds by a scale factor. Two scale factors were considered: one 2 times smaller (scale factor $\alpha = 0.5$) and the other 2 times larger ($\alpha = 2.0$). The simulation using these adjustments showed their strong effect on the cloud organization. For the smaller-scale factor, the number of small cells was very high, higher than for the simulation with 1D turbulence. For scale factor $\alpha = 2.0$, the number of cloud cells was drastically reduced, showing the importance of a better determination of this scale factor according to the cloud size.

The innovative methodology presented in this study allows us to evaluate the skill of the model in describing the space–time organization of cloud and rainfall. Using this methodology, we confirmed the results obtained by Caine et al. (2013) and Hanley et al. (2015) that in general the so-called cloud-resolving models produce more small cloud systems and rain cells than observed in reality. It was also possible to test the effect of different turbulent parameterizations and mixing lengths. The mixing length affected the cloud organization, particularly when it was changed inside clouds. This result suggests that adjustment of this parameter can result in a much better description of the cloud and rain fields. However, this study should be applied to other cloud regimes to check the overall result.

The importance of the model grid resolution on the cloud organization was not investigated here. The same analysis done here for different turbulent parameterizations and mixing lengths could be extended to changes in the resolution. As mentioned in the introduction, the simulation of deep convective storms has been found to be very sensitive to the grid spacing (e.g., Bryan et al. 2003; Khairoutdinov et al. 2009; Fiori et al. 2010; Bryan and Morrison 2012; Caine et al. 2013; Dauhut et al. 2015; Hanley et al. 2015; Verrelle et al. 2015). Another aspect that remains to be examined is the sensitivity of the results to the microphysics formulation. Indeed, changes to microphysics can have a qualitatively similar impact on structure and intensity of convective storm than a change in grid spacing (e.g., Bryan and Morrison 2012).

Acknowledgments. This work was supported by FAPESP Grant 2009/15235-8, the CHUVA Project, and CNPQ 242659/2012-8. Part of this work was carried out at the Observatoire Midi-Pyrénées–Laboratoire d'Aérologie. The authors also thank all the participants in the CHUVA-SUL field campaign.

REFERENCES

Bechtold, P., E. Bazile, F. Guichard, P. Mascart, and E. Richard, 2001: A mass flux convection scheme for regional and global models. *Quart. J. Roy. Meteor. Soc.,* **127,** 869–886, doi:10.1002/qj.49712757309.

Bougeault, P., and P. Lacarrère, 1989: Parameterization of orography-induced turbulence in a meso-beta-scale model. *Mon. Wea. Rev.,* **117,** 1872–1890, doi:10.1175/1520-0493(1989)117<1872:POOITI>2.0.CO;2.

Bryan, G. H., and H. Morrison, 2012: Sensitivity of a simulated squall line to horizontal resolution and parameterization of microphysics. *Mon. Wea. Rev.,* **140,** 202–225, doi:10.1175/MWR-D-11-00046.1.

——, J. C. Wyngaard, and J. M. Fritsch, 2003: Resolution requirements for the simulation of deep moist convection. *Mon. Wea. Rev.,* **131,** 2394–2416, doi:10.1175/1520-0493(2003)131<2394:RRFTSO>2.0.CO;2.

Caine, S., T. P. Lane, P. T. May, C. Jakob, S. T. Siems, M. J. Manton, and J. Pinto, 2013: Statistical assessment of tropical

convection-permitting model simulations using a cell-tracking algorithm. *Mon. Wea. Rev.,* **141,** 557–581, doi:10.1175/MWR-D-11-00274.1.

Cecil, D. J., and C. B. Blankenship, 2012: Toward a global climatology of severe hailstorms as estimated by satellite passive microwave imagers. *J. Climate,* **25,** 687–703, doi:10.1175/JCLI-D-11-00130.1.

Chaboureau, J.-P., and P. Bechtold, 2005: Statistical representation of clouds in a regional model and the impact on the diurnal cycle of convection during Tropical Convection, Cirrus and Nitrogen Oxides (TROCCINOX). *J. Geophys. Res.,* **110,** D17103, doi:10.1029/2004JD005645.

——, and J.-P. Pinty, 2006: Validation of a cirrus parameterization with Meteosat Second Generation observations. *Geophys. Res. Lett.,* **33,** L03815, doi:10.1029/2005GL024725.

——, and Coauthors, 2008: A midlatitude cloud database validated with satellite observations. *J. Appl. Meteor. Climatol.,* **47,** 1337–1353, doi:10.1175/2007JAMC1731.1.

Chong, M., P. Amayenc, G. Scialom, and J. Testud, 1987: A tropical squall line observed during the COPT 81 Experiment in West Africa. Part I: Kinematic structure inferred from dual-Doppler radar data. *Mon. Wea. Rev.,* **115,** 670–694, doi:10.1175/1520-0493(1987)115<0670:ATSLOD>2.0.CO;2.

Cuxart, J., P. Bougeault, and J.-L. Redelsperger, 2000: A turbulence scheme allowing for mesoscale and large-eddy simulations. *Quart. J. Roy. Meteor. Soc.,* **126,** 1–30, doi:10.1002/qj.49712656202.

Dauhut, T., J.-P. Chaboureau, J. Escobar, and P. Mascart, 2015: Large-eddy simulation of Hector the convector making the stratosphere wetter. *Atmos. Sci. Lett.,* **16,** 135–140, doi:10.1002/asl2.534.

Del Genio, A. D., and J. Wu, 2010: The role of entrainment in the diurnal cycle of continental convection. *J. Climate,* **23,** 2722–2738, doi:10.1175/2009JCLI3340.1.

Emanuel, K. A., 1994: Theory of mixing in cumulus clouds. *Atmospheric Convection,* Oxford University Press, 215–229.

Fiori, E., A. Parodi, and F. Siccardi, 2010: Turbulence closure parameterization and grid spacing effects in simulated supercell storms. *J. Atmos. Sci.,* **67,** 3870–3890, doi:10.1175/2010JAS3359.1.

Fouquart, Y., and B. Bonnel, 1986: Computations of solar heating of the Earth's atmosphere: A new parametrization. *Beitr. Phys. Atmos.,* **53,** 35–62.

Hanley, K. E., R. S. Plant, T. H. M. Stein, R. J. Hogan, J. C. Nicol, H. W. Lean, C. Halliwell, and P. A. Clark, 2015: Mixing-length controls on high-resolution simulations of convective storms. *Quart. J. Roy. Meteor. Soc.,* **141,** 272–284, doi:10.1002/qj.2356.

Honnert, R., V. Masson, and F. Couvreux, 2011: A diagnostic for evaluating the representation of turbulence in atmospheric models at the kilometric scale. *J. Atmos. Sci.,* **68,** 3112–3131, doi:10.1175/JAS-D-11-061.1.

Jensen, M. P., and A. D. Del Genio, 2006: Factors limiting convective cloud-top height at the ARM Nauru Island climate research facility. *J. Climate,* **19,** 2105–2117, doi:10.1175/JCLI3722.1.

Kain, J. S., and J. M. Fritsch, 1993: Convective parameterization for mesoscale models: The Kain–Fritsch scheme. *The Representation of Cumulus Convection in Numerical Models, Meteor. Monogr.,* No. 46, Amer. Meteor. Soc., 165–170.

Khairoutdinov, M. F., S. K. Krueger, C.-H. Moeng, P. A. Bogenschutz, and D. A. Randall, 2009: Large-eddy simulation of maritime deep tropical convection. *J. Adv. Model. Earth Syst.,* **1** (15), doi:10.3894/JAMES.2009.1.15.

Kidd, C., E. Dawkins, and G. Huffman, 2013: Comparison of precipitation derived from the ECMWF operational forecast model and satellite precipitation datasets. *J. Hydrometeor.,* **14,** 1463–1482, doi:10.1175/JHM-D-12-0182.1.

Lafore, J. P., and Coauthors, 1998: The Meso-NH Atmospheric Simulation System. Part I: Adiabatic formulation and control simulations. *Ann. Geophys.,* **16,** 90–109, doi:10.1007/s00585-997-0090-6.

Lu, C., Y. Liu, S. Niu, S. Krueger, and T. Wagner, 2013: Exploring parameterization for turbulent entrainment-mixing processes in clouds. *J. Geophys. Res. Atmos.,* **118,** 185–194, doi:10.1029/2012JD018464.

Machado, L. A. T., W. B. Rossow, R. L. Guedes, and A. W. Walker, 1998: Life cycle variations of mesoscale convective systems over the Americas. *Mon. Wea. Rev.,* **126,** 1630–1654, doi:10.1175/1520-0493(1998)126<1630:LCVOMC>2.0.CO;2.

——, H. Laurent, and A. A. Lima, 2002: Diurnal march of the convection observed during TRMM-WETAMC/LBA. *J. Geophys. Res.,* **107,** 8064, doi:10.1029/2001JD000338.

——, W. F. S. Lima, O. Pinto Jr., and C. B. Morales, 2009: Relationship between cloud-ground discharge and penetrative clouds: A multi-channel satellite application. *Atmos. Res.,* **93,** 304–309, doi:10.1016/j.atmosres.2008.10.003.

——, and Coauthors, 2014: The Chuva Project: How does convection vary across Brazil? *Bull. Amer. Meteor. Soc.,* **95,** 1365–1380, doi:10.1175/BAMS-D-13-00084.1.

Mapes, B. E., and R. B. Neale, 2011: Parameterizing convective organization to escape the entrainment dilemma. *J. Adv. Model. Earth Syst.,* **3,** M06004, doi:10.1029/2011MS000042.

Meehl, G. A., F. Zwiers, J. Evans, T. Knutson, L. Mearns, and P. Whetton, 2000: Trends in extreme weather and climate events: Issues related to modeling extremes in projections of future climate change. *Bull. Amer. Meteor. Soc.,* **81,** 427–436, doi:10.1175/1520-0477(2000)081<0427:TIEWAC>2.3.CO;2.

Meirold-Mautner, I., C. Prigent, E. Defer, J.-R. Pardo, J.-P. Chaboureau, J.-P. Pinty, M. Mech, and S. Crewell, 2007: Radiative transfer simulations using mesoscale cloud model outputs: Comparisons with passive microwave and infrared satellite observations for midlatitudes. *J. Atmos. Sci.,* **64,** 1550–1568, doi:10.1175/JAS3896.1.

Mlawer, E. J., S. J. Taubman, P. D. Brown, M. J. Iacono, and S. A. Clough, 1997: Radiative transfer for inhomogeneous atmospheres: RRTM, a validated correlated-k model for the longwave. *J. Geophys. Res.,* **102,** 16 663–16 682, doi:10.1029/97JD00237.

Morrison, H., and W. W. Grabowski, 2007: Comparison of bulk and bin warm-rain microphysics models using a kinematic framework. *J. Atmos. Sci.,* **64,** 2839–2861, doi:10.1175/JAS3980.

Negri, R. G., L. A. T. Machado, S. English, and M. Forsythe, 2014: Combining cloud resolving model with satellite for cloud process model simulation validation. *J. Appl. Meteor. Climatol.,* **53,** 521–533, doi:10.1175/JAMC-D-12-0178.1.

Pergaud, J., V. Masson, S. Malardel, and F. Couvreux, 2009: A parameterization of dry thermals and shallow cumuli for mesoscale numerical weather prediction. *Bound.-Layer Meteor.,* **132,** 83–106, doi:10.1007/s10546-009-9388-0.

Pinty, J.-P., and P. Jabouille, 1998: A mixed-phase cloud parameterization for use in mesoscale non-hydrostatic model: Simulations of a squall line and of orographic precipitations. *Proc. Conf. on Cloud Physics,* Everett, WA, Amer. Meteor. Soc., 217–220.

Richard, E., S. Cosma, P. Tabary, J.-P. Pinty, and M. Hagen, 2003: High-resolution numerical simulations of the convective system observed in the Lago Maggiore area on 17 September

1999 (MAP IOP 2a). *Quart. J. Roy. Meteor. Soc.,* **129,** 543–563, doi:10.1256/qj.02.50.

Ringer, M. A., J. M. Edwards, and A. Slingo, 2003: Simulation of satellite channel 18 radiances in the Met Office Unified model. *Quart. J. Roy. Meteor. Soc.,* **129,** 1169–1190, doi:10.1256/qj.02.61.

Rosenfeld, D., W. L. Woodley, A. Lerner, G. Kelman, and D. T. Lindsey, 2008: Satellite detection of severe convective storms by their retrieved vertical profiles of cloud particle effective radius and thermodynamic phase. *J. Geophys. Res.,* **113,** D04208, doi:10.1029/2007JD008600.

Salio, P., M. Nicolini, and E. J. Zipser, 2007: Mesoscale convective systems over southeastern South America and their relationship with the South American low-level jet. *Mon. Wea. Rev.,* **135,** 1290–1309, doi:10.1175/MWR3305.1.

Saunders, R., M. Matricardi, P. Brunel, S. English, P. Bauer, U. O'Keeffe, P. Francis, and P. Rayer, 2005: RTTOV-8 science and validation report. Tech. Rep., NWP SAF Rep., 41 pp.

Shrestha, D. L., D. E. Robertson, Q. J. Wang, T. C. Pagano, and H. A. P. Hapuarachchi, 2013: Evaluation of numerical weather prediction model precipitation forecasts for short-term streamflow forecasting purpose. *Hydrol. Earth Syst. Sci.,* **17,** 1913–1931, doi:10.5194/hess-17-1913-2013.

Simpson, J., 1971: On cumulus entrainment and one-dimensional models. *J. Atmos. Sci.,* **28,** 449–455, doi:10.1175/1520-0469(1971)028<0449:OCEAOD>2.0.CO;2.

Söhne, N., J.-P. Chaboureau, and F. Guichard, 2008: Verification of cloud cover forecast with satellite observation over West Africa. *Mon. Wea. Rev.,* **136,** 4421–4434, doi:10.1175/2008MWR2432.1.

Stein, J., E. Richard, J.-P. Lafore, J.-P. Pinty, N. Asencio, and S. Cosma, 2000: High-resolution non-hydrostatic simulations of flash-flood episodes with grid-nesting and ice-phase parametrization. *Meteor. Atmos. Phys.,* **72,** 203–221, doi:10.1007/s007030050016.

Varble, A., and Coauthors, 2011: Evaluation of cloud-resolving model intercomparison simulations using TWP-ICE observations: Precipitation and cloud structure. *J. Geophys. Res.,* **116,** D12206, doi:10.1029/2010JD015180.

——, and Coauthors, 2014: Evaluation of cloud-resolving and limited area model intercomparison simulations using TWP-ICE observations. 1: Deep convective updraft properties. *J. Geophys. Res. Atmos.,* **119,** 13 891–13 918, doi:10.1002/2013JD021371.

Verrelle, A., D. Ricard, and C. Lac, 2015: Sensitivity of high-resolution idealized simulations of thunderstorms to horizontal resolution and turbulence parameterization. *Quart. J. Roy. Meteor. Soc.,* **141,** 433–448, doi:10.1002/qj.2363.

Vila, D. A., L. A. T. Machado, H. Laurent, and I. Velasco, 2008: Forecast and Tracking the Evolution of Cloud Clusters (ForTraCC) using satellite infrared imagery: Methodology and validation. *Wea. Forecasting,* **23,** 233–245, doi:10.1175/2007WAF2006121.1.

Wang, Y., L. Zhou, and K. P. Hamilton, 2007: Effect of convective entrainment/detrainment on simulation of tropical precipitation diurnal cycle. *Mon. Wea. Rev.,* **135,** 567–585, doi:10.1175/MWR3308.1.

Wu, J., A. D. Del Genio, M.-S. Yao, and A. B. Wolf, 2009: WRF and GISS SCM simulations of convective updraft properties during TWP-ICE. *J. Geophys. Res.,* **114,** D04206, doi:10.1029/2008JD010851.